CHEMISTRY OF MATERIALS

ARTICLE

pubs.acs.org/cm

Structural, Thermal, and Physical Properties of the Thallium Zirconium Telluride Tl_2ZrTe_3

Cheriyedath Raj Sankar, Mykhailo Guch, Abdeljalil Assoud, and Holger Kleinke*

Department of Chemistry, University of Waterloo, Waterloo, Ontario N2L 3G1, Canada

Supporting Information

ABSTRACT: We have synthesized Tl_2ZrTe_3 at elevated temperatures starting from the elements. Tl_2ZrTe_3 adopts a cubic structure, space group $P2_13$ with a unit cell parameter of a = 19.118(1) Å (Z = 36). All Tl and Zr atoms are octahedrally (distorted) coordinated by Te atoms. One out of 11 crystallographically distinct Te atoms in the structure is not connected to any Zr atoms, but is surrounded by six Tl atoms in the form of a severely distorted octahedron. Because of the absence of any significant homonuclear interactions, all atoms are in their most common oxidation states, namely, Tl^+, Zr^{4+}, and Te^{2-}. Electronic structure calculations and physical property measurements reveal the semiconducting characteristics of the compound. The structure and thermoelectric properties of Tl_2ZrTe_3 and Tl_2SnTe_3 are compared in the present work. The dimensionless figure of merit, ZT, was found to be 0.18 for Tl_2ZrTe_3 at 420 K and 0.31 for Tl_2SnTe_3 at 500 K, with both materials exhibiting very low thermal conductivity. Tl_2ZrTe_3 decomposes irreversibly around 450 K in open systems under inert gas atmosphere, while it remains stable up to its incongruent melting point at 835 K in closed silica tubes.

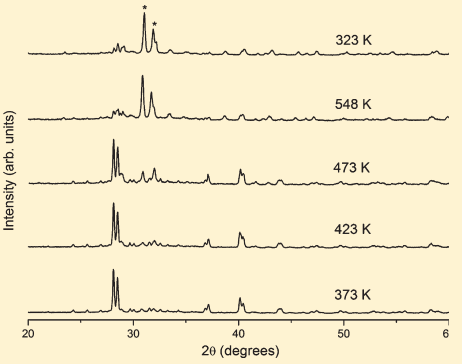

KEYWORDS: crystal structure, single crystal X-ray diffraction, thallium chalcogenide, electronic structure, thermoelectric, semiconductor

INTRODUCTION

Some of the most efficient thermoelectric materials known to date are heavy metal chalcogenides and antimonides. The thermoelectric efficiency of a material is related to the Seebeck coefficient (S), the electrical conductivity (σ), and the thermal conductivity (κ) of that material, and is often expressed in terms of the dimensionless figure of merit, ZT, which is given by $ZT = TS^2\sigma/\kappa$.[1−4] Thermoelectric materials are potential candidates for heat to electricity conversion, not only to harvest electrical energy from the waste heat but also to use them in solar-thermal-electric energy conversion technology.[5] For this, the efficiency of such materials should be enhanced. An important criterion for such candidate materials is that the compound should be a narrow-band gap semiconductor.

Several new narrow-band gap semiconducting materials with reasonable thermoelectric efficiency have been identified during the past several years. Ternary thallium chalcogenides form an important class of such materials. The incorporation of the heavy element thallium often occurs with a low lattice contribution to the thermal conductivity.[6−15] Also, Tl^+ ion can be influential on the material's physical properties owing to the stereochemically active lone pair of the 6s electrons and consequent complexities in structure and bonding. Recently, we reported the structure, bonding, and thermoelectric properties of two new thallium-group4-tellurides, Tl_4MTe_4 (M = Zr and Hf).[16] Further investigation in this ternary system led us to investigate the structural and thermoelectric behavior of another material, Tl_2ZrTe_3. The existence of this telluride has been uncovered in an earlier report on phase studies of the Tl_2Q-ZrQ_2 systems (Q = S, Se, Te).[17] For comparison, we analyzed the physical properties of Tl_2ZrTe_3 with the corresponding Sn counterpart, Tl_2SnTe_3,[18] which has a different structure.

Tl_2GeTe_3[19] and Tl_2SnTe_3[18] crystallize in the orthorhombic space group *Pnma* with $[GeTe_4]/[SnTe_4]$ tetrahedra and $[TlTe_8]$ square antiprisms. These compounds show interesting thermoelectric properties.[11,13] The alkali metal (A) compounds A_2ZrTe_3 are isostructural, crystallize in the monoclinic space group $P2_1/c$, and contain infinite chains of face-condensed $[ZrTe_6]$ octahedra with A = K or Rb.[20] Moreover, Cu_2ZrTe_3 and Cu_2HfTe_3 are isostructural with space group $C2/m$ and show a metallic-like temperature dependence of the electrical conductivity,[21] presumably because of the deficiency of cations in an otherwise semiconductor.[22] Other related chalcogenides are $ACuZrQ_3$[23] and $TlCuMQ_3$[24] (A = K or Na, M = Zr or Hf, Q = S or Se), which share common structural features, for example, edge-sharing $[MQ_6]$ octahedra, and crystallize in the orthorhombic space group *Cmcm*.

EXPERIMENTAL SECTION

Synthesis and Phase Purity Analysis. The compounds were synthesized from the respective elements stored in an argon-filled

Received: April 7, 2011
Revised: July 28, 2011
Published: August 09, 2011

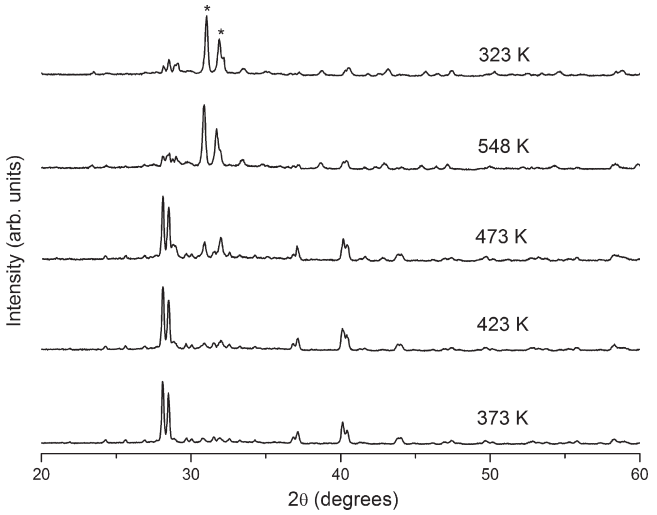

Figure 1. Temperature dependent X-ray diagrams, beginning with a pure Tl_2ZrTe_3 sample. The sample was heated from 373 to 423 K to 473 to 548 K, and the last pattern was obtained after cooling down to 323 K.

glovebox (Tl granules, 99.9% (Alfa Aesar); Zr powder −325 mesh, 98.5% (Alfa Aesar); Hf powder −100 mesh, 99.6% (Alfa Aesar); Sn powder, 99.9% (Alfa Aesar); and Te chunks, 99.9% (Aldrich)). To synthesize Tl_2ZrTe_3, the required stoichiometric amounts of the individual elements were weighed into a glassy carbon crucible, which were then introduced into a quartz ampule and sealed under vacuum. The ampule was heated slowly to 1073 K in a resistance furnace, allowed to remain at 1073 K for 100 h, slowly cooled down to 773 K, held at 773 K for 300 h and finally slowly cooled down to room temperature. This annealing temperature was chosen because Tl_2ZrTe_3 was reported to undergo a peritectic reaction at 805 K into solid $ZrTe_2$ and liquid,[17] which was slightly higher in our DSC experiments, namely, at 835 K. Protecting the sample from reacting with the silica by shielding it with the glassy carbon crucible avoids the incorporation of Si into the products, but is not required for the formation of Tl_2ZrTe_3 as the main product.

To synthesize Tl_2SnTe_3, the use of a crucible within the silica tube was not necessary. This ampule was heated slowly to 923 K, held at 923 K for 24 hours, cooled to 523 K within 200 hours, and then the furnace was switched off.

To analyze the sample purities, powder X-ray diffraction experiments of the samples were performed using an Inel powder diffractometer with position-sensitive detector and Cu-$K\alpha_1$ radiation. Our attempts to synthesize the corresponding hafnium compound, however, were not successful at various reaction conditions. Tl_4HfTe_4 with some unknown phases or $HfTe_2$ and Tl_2Te were the major products of such reactions, depending on the reaction conditions.

The Tl_2ZrTe_3 sample was found to be stable in air. Its thermal stability was studied via differential scanning calorimetry (DSC) using the Netzsch STA 409PC Luxx under a stream of argon. The DSC experiment revealed the presence $Tl_{5-x}Zr_xTe_3$ (not found prior to this experiment) via its melting point around 720 K, and an incongruent melting temperature of the Tl_2ZrTe_3 at 835 K, somewhat consistent with the above-mentioned phase diagram studies. The powder XRD pattern of the post-DSC sample showed the existence of $Tl_{5-x}Zr_xTe_3$, Tl_2ZrTe_3, and $ZrTe_2$.

Further, our high temperature powder XRD studies using the above-mentioned Inel machine up to 548 K under a flow of helium suggest decomposition of the sample, yielding Tl_5Te_3 (or $Tl_{5-x}Zr_xTe_3$) as the major product, beginning as early as 473 K (main peaks marked with * in Figure 1). In this experiment, powder patterns were measured each over a period of 20 min at 373 K, 423 K, 473 K, 548 K, 473 K, 423 K, 373 K, and finally at 323 K, with the whole experiment taking about 6 h including the heating and cooling periods. This decomposition appeared to be irreversible in this open system experiment, as the powder diagram at 323 K, obtained after cooling down, revealed; no change was observed during the cooling process.

Table 1. Crystallographic Information of Tl_2ZrTe_3

empirical formula	Tl_2ZrTe_3
formula weight [g/mol]	882.76
temperature [K]	298(2)
wavelength [Å]	0.71073
crystal system	cubic
space group	$P2_13$
unit cell dimensions [Å]	a = 19.118(1)
volume [Å^3], Z	6987.5(9), 36
density (calculated) [g/cm^3]	7.552
goodness-of-fit on F^2	1.103
no. of reflections: total, unique, observed	66058, 6788, 6045
final R indices [$I > 2\sigma(I)$]	R1 = 0.0387, wR2 = 0.0602
R indices (all data)	R1 = 0.0481, wR2 = 0.0644

On the other hand, no decomposition of Tl_2ZrTe_3 was observed by heating the sample up to 573 K, followed by furnace cooling in a closed silica ampule. Thus, we believe that a slight amount of tellurium evaporates from Tl_2ZrTe_3 during the heating cycle in an open system, causing decomposition of the sample, noting that the Te content of the major product $Tl_{5-x}Zr_xTe_3$ is smaller than in the starting material, Tl_2ZrTe_3. Assuming another product is $ZrTe_2$, eq 1 is reasonable as long as $1/3 < x \leq 5/3$:

$$(5-x)Tl_2ZrTe_3 \rightarrow 2Tl_{5-x}Zr_xTe_3 + (5-3x)ZrTe_2 + (3x-1)Te \quad (1)$$

Single-Crystal Structure Determination. A suitable single-crystal (rectangular block) was picked from the bulk sample for the single-crystal X-ray diffraction analysis. The data were collected at room temperature, by using a Bruker Smart Apex CCD diffractometer that employs Mo-$K\alpha$ radiation, by scans of 0.3° in ω at two different φ angles with exposure times of 30 s each for a total of 2 × 600 frames. The data were treated for Lorentz and polarization corrections. The absorption corrections were based on fitting a function to the empirical transmission surface as sampled by multiple equivalent measurements. The data reduction and structure refinement were carried out within the APEX2 software package.[25]

The structure was solved and refined in space group $P2_13$. The unit cell consists of 36 formula units of Tl_2ZrTe_3. The final R1 and wR2 values ($I > 2\sigma$) were found to be 0.0387 and 0.0602, respectively. The crystallographic details are given in Table 1. The displacement parameters (U_{eq}) for the Tl sites varied from 0.027 Å^2 to 0.033 Å^2; refining the occupancies of the sites with U_{eq} > 0.03 Å^2 (Tl1, Tl2, Tl8) afforded identical R values as before, with 99.3(3)%, 98.8(3)%, and 99.8(5)% occupation of Tl1, Tl2, and Tl8, respectively. Similarly, as three Te sites exhibited U_{eq} values of 0.019 Å^2 (Te4), 0.020 Å^2 (Te6), and 0.023 Å^2 (Te9), compared to 0.013 Å^2 to 0.016 Å^2 of the other Te sites, their occupancies were tentatively refined as well to check for Te deficiencies. Again, no changes in the R values were detected, and the refined occupancies were 1.000(4) for Te4 and Te6 and 1.010(7) for Te9. All these slight variations can, however, be considered insignificant, as they are within four times their standard deviations, and thus no deficiencies were considered in the final structure model. Finally, the PLATON package was used to check for additional symmetry (ADDSYM) and to obtain standardized atomic positions (TIDY).[26]

Electronic Structure Calculation. The very large unit cell of Tl_2ZrTe_3 with its 216 atoms prohibited an LMTO (tight binding Linear Muffin-Tin Orbital) method of electronic structure calculation, which we used on Tl_4ZrTe_4. Thus, the extended Hückel tight binding (EHTB)

Table 2. Atomic Parameters Used for EHTB Calculations

atom	orbital	H_{ii} [eV]	ζ_1	ζ_2	c_1	c_2
Tl	6s	−16.20	2.37		1	
	6p	−9.000	1.97		1	
Zr	5s	−8.204	1.82		1	
	5p	−4.593	1.78		1	
	4d	−8.117	3.84	1.51	0.6213	0.5798
Te	5s	−20.80	2.51		1	
	5p	−13.20	2.16		1	

method using the CAESAR (Crystal and Electronic Structure Analyzer) package from Prime Color was employed for the electronic structure calculation of Tl_2ZrTe_3.[27] In EHTB, valence orbitals are approximated as Slater-type orbitals (STO), and the valence state ionization potentials (VSIP) and STO exponents used are listed in Table 2. c_1 and c_2 are the coefficients of single and double-ζ STO's represented by ζ_1 and ζ_2, respectively. We optimized the VISP parameters for Zr via charge iterations on $ZrTe_2$, and used reported Tl parameters.[28]

The electronic structure of Tl_2SnTe_3 was calculated by using the LMTO method that uses the atomic spheres approximation (ASA).[29,30] Therein, density functional theory (DFT) is employed, which utilizes the local density approximation for the exchange and correlation energies. The crystallographic information file for Tl_2SnTe_3 was obtained from the ICDD file number 69562.[18] The following wave functions were used for the calculation: for Tl, 6s, 6p, and included via the downfolding technique[31] 6d and 5f, for Sn and Te, 5s, 5p, 5d (downfolded) and 4f (downfolded).

Physical Property Measurements. Physical property measurements reported in this paper were all measured on pressed bulk powder samples. For electrical transport measurements, the samples were pressed into rectangular pellets of the dimensions 13 × 2 × 2 mm by applying a force of 20 kN, which corresponds to a pressure of 770 MPa. For the thermal diffusivity measurements, disk-shaped pellets with a diameter of 8 mm and a thickness of 1.6 mm−2 mm were pressed under a force of 40 kN, corresponding to a pressure of 800 MPa. Prior to the measurements, all the pressed pellets were sintered for 48 h in vacuum sealed quartz tubes, namely, at 723 K in case of Tl_2ZrTe_3 and at 523 K in case of Tl_2SnTe_3. Densities of 90% of the theoretical maximum (deduced from the X-ray data) were obtained for both pellets of Tl_2ZrTe_3, and 93% for Tl_2SnTe_3.

The electrical transport measurements were carried out on an ULVAC ZEM-3 measurement unit that measures both the Seebeck coefficient (S) and the electrical conductivity (σ) (by a four-probe method) as a function of temperature. Thermal diffusivity (α) of the samples was determined by using Anter Flashline 3000 that employs a flash method. Thermal conductivity (κ) was calculated from the thermal diffusivity via $\kappa = \rho\,\alpha\,C_P$ by using the Dulong−Petit limit for the specific heat capacity (C_P), with ρ being the experimentally measured density.

Both these measurements were performed under inert gas (flow of argon during the diffusivity and about 0.9 kPa of helium during the Seebeck/conductivity measurement); the Tl_2ZrTe_3 sample was decomposed after the measurement. In view of our high temperature X-ray measurements, it is concluded that the data obtained on "Tl_2ZrTe_3" above 450 K stem from a mixture of decomposition products and are thus irrelevant for the properties of the compound Tl_2ZrTe_3. These data are shown in this manuscript, highlighted with a dashed line.

RESULTS AND DISCUSSION

Crystal Structure. The unit cell of Tl_2ZrTe_3 (Figure 2) contains a three-dimensional (3D) infinite network of edge-sharing [$ZrTe_6$] octahedra. There are three crystallographically distinct Zr atoms, each of which forms six Zr−Te bonds with distances ranging from 2.82 Å to 3.05 Å (Table 3). The

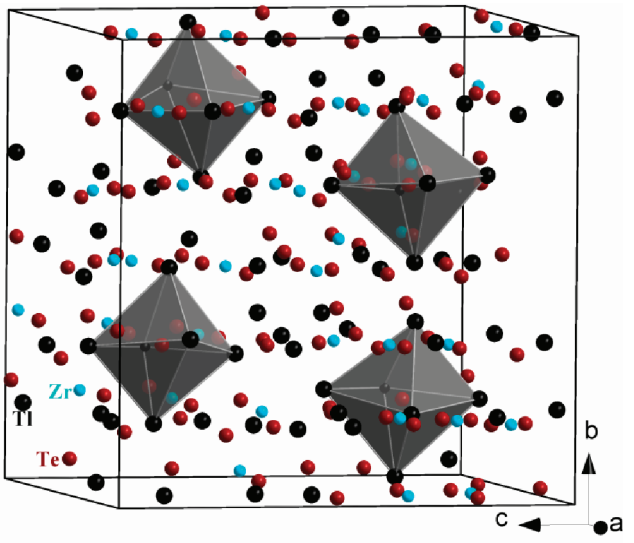

Figure 2. Unit cell of Tl_2ZrTe_3, emphasizing the [$Te9Tl_6$] octahedra.

Table 3. Selected Interatomic Distances [Å]

Tl1−Te9	3.164(1)	Tl2−Te6		3.228(1)
Tl1−Te1	3.385(1)	Tl2−Te4		3.255(1)
Tl1−Te3	3.413(1)	Tl2−Te4		3.403(1)
Tl1−Te7	3.502(1)	Tl2−Te8		3.431(1)
Tl1−Te1	3.509(1)	Tl2−Te11		3.623(1)
Tl1−Te2	3.567(1)	Tl2−Te5		3.645(1)
Tl3−Te9	3.234(1)	Tl4−Te1		3.234(1)
Tl3−Te6	3.265(1)	Tl4−Te6		3.260(1)
Tl3−Te2	3.288(1)	Tl4−Te4		3.279(1)
Tl3−Te6	3.356(1)	Tl4−Te2		3.461(1)
Tl3−Te3	3.461(1)	Tl4−Te3		3.484(1)
Tl3−Te5	3.519(1)	Tl4−Te7		3.565(1)
Tl5−Te3	3.187(1)	Tl6−Te4	3×	3.262(1)
Tl5−Te8	3.228(1)	Tl6−Te1	3×	3.477(1)
Tl5−Te4	3.299(1)			
Tl5−Te8	3.453(1)	Tl7−Te6	3×	3.306(1)
Tl5−Te10	3.466(1)	Tl7−Te8	3×	3.465(1)
Tl5−Te5	3.493(1)			
		Tl8−Te2	3×	3.257(1)
		Tl8−Te7	3×	3.696(1)
Zr1−Te1	2.865(2)			
Zr1−Te2	2.893(2)	Zr2−Te6		2.826(2)
Zr1−Te2	2.897(2)	Zr2−Te4		2.829(2)
Zr1−Te5	2.914(2)	Zr2−Te1		2.908(2)
Zr1−Te3	2.927(2)	Zr2−Te8		2.926(2)
Zr1−Te10	2.998(2)	Zr2−Te7		2.986(2)
		Zr2−Te5		3.049(2)
Zr3−Te8	2.838(2)			
Zr3−Te3	2.878(2)			
Zr3−Te7	2.910(2)			
Zr3−Te5	2.921(2)			
Zr3−Te7	2.945(2)			
Zr3−Te11	2.947(2)			

dx.doi.org/10.1021/cm200994t |*Chem. Mater.* 2011, 23, 3886–3891

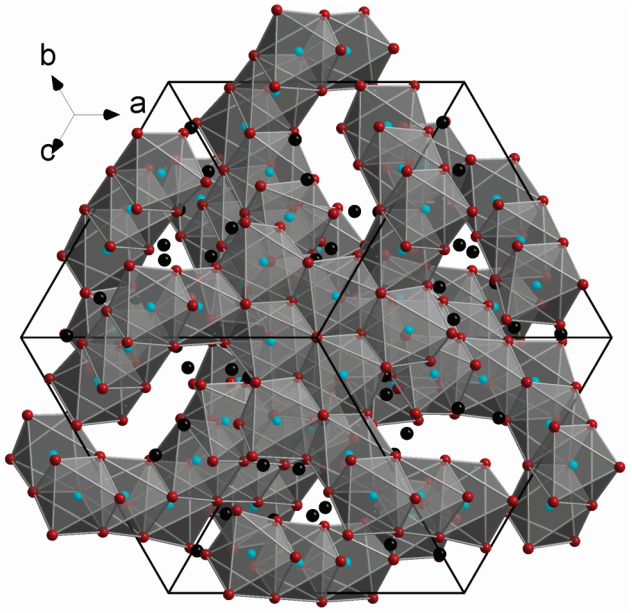

Figure 3. 3D arrangement of edge-sharing $[ZrTe_6]$ octahedra of Tl_2ZrTe_3.

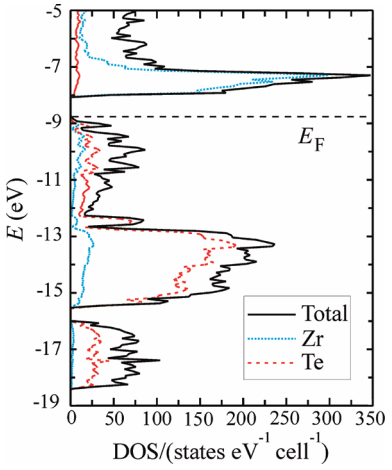

Figure 4. Densities of states (DOS) of Tl_2ZrTe_3, calculated via the EHTB method.

propagation of the edge-sharing $[ZrTe_6]$ octahedra along the [111] direction is shown in Figure 3. The Zr−Te distances found in Tl_2ZrTe_3 are similar to those in Tl_4ZrTe_4.[16] However, in Tl_4ZrTe_4, $[ZrTe_6]$ octahedra are face-condensed and assembled into trimeric $[Zr_3Te_{12}]$ units. As a result, a weak Zr−Zr interaction (3.63 Å) can be envisaged in Tl_4ZrTe_4, and another slightly stronger interaction of 3.46 Å in nonstoichiometric $Tl_4Zr_{1+x}Te_4$. The Zr−Zr distances in elemental Zr range from 3.18 Å to 3.23 Å. In contrast, no Zr−Zr distances in Tl_2ZrTe_3 are shorter than 4.1 Å, clearly indicating absence of any interaction.

The structure contains eight different Wyckoff positions for the Tl atoms. Here, the Tl−Tl interactions are apparently rather weak, as can be learned from the Tl−Tl distances of around 4.00 Å. This is different in many binary and other ternary thallium tellurides such as Tl_5Te_3,[32] Tl_4ZrTe_4,[16] and $Tl_6Si_2Te_6$,[33] for which Tl−Tl interactions vary from 3.49 Å to 4.00 Å and are extended in three dimensions. For comparison, the Tl−Tl distances of the hexagonal modification of elemental Tl are 3.41 Å and 3.46 Å.

Tl−Te interactions occur in the range of 3.16 Å to 4.04 Å, with the Tl atoms each coordinated by six Te atoms in form of irregular octahedra. The irregularity can be explained with the stereochemical activity of the $6s^2$ lone pair of electrons of the Tl^+ ions. The $[TlTe_6]$ octahedra are also edge-shared and extend throughout the structure in a 3D fashion.

A special feature of the structure is the coordination environment of one of the 11 distinct Te sites. Te9 is not involved in bonding with Zr atoms; rather, it centers a $[Te9Tl_6]$ octahedron with Te9−Tl1 and Te9−Tl3 bonds of 3.16 Å and 3.23 Å, the former being the shortest Tl−Te interaction of this structure. Te9 has its nearest Te neighbor at a distance of >4.60 Å and is thus not involved in any Te−Te interactions. Similar features also occurred in $Ba_7Sn_3Se_{13}$ and $NaBa_6Cu_3Te_{14}$, wherein at least one of the chalcogenide sites is coordinated to only Ba atoms.[34,35]

The other compound included in the present study, Tl_2SnTe_3 with Sn in lieu of Zr, crystallizes in the orthorhombic space group *Pnma*.[18] Assigning the oxidation states for Tl_2ZrTe_3 and Tl_2SnTe_3 is straightforward, with all the constituent atoms exhibiting their most common oxidation states (Tl^+, Zr^{4+}, Sn^{4+}, Te^{2-}). The crystal structure of Tl_2SnTe_3 consists of double sheets of $[SnTe_4]$ tetrahedra and $[TlTe_8]$ square antiprisms stitched together, two such

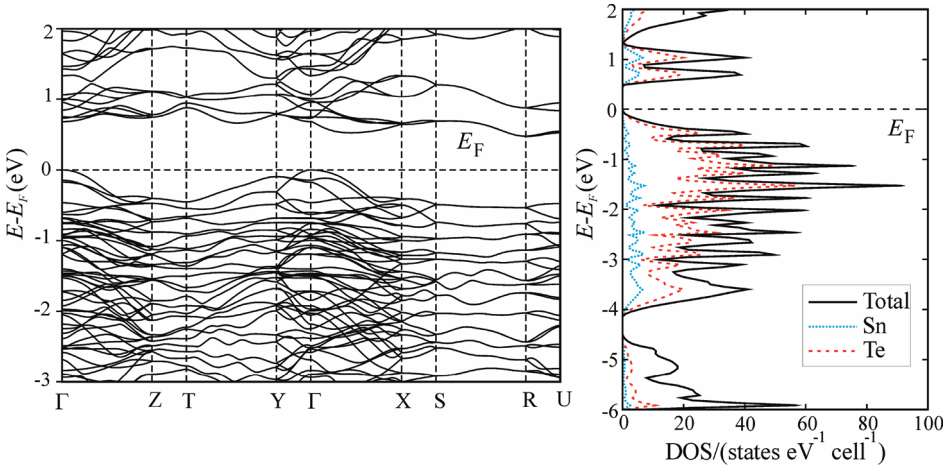

Figure 5. Band structure (left) and densities of states (right) of Tl_2SnTe_3, calculated via the LMTO method.

dx.doi.org/10.1021/cm200994t |*Chem. Mater.* 2011, 23, 3886–3891

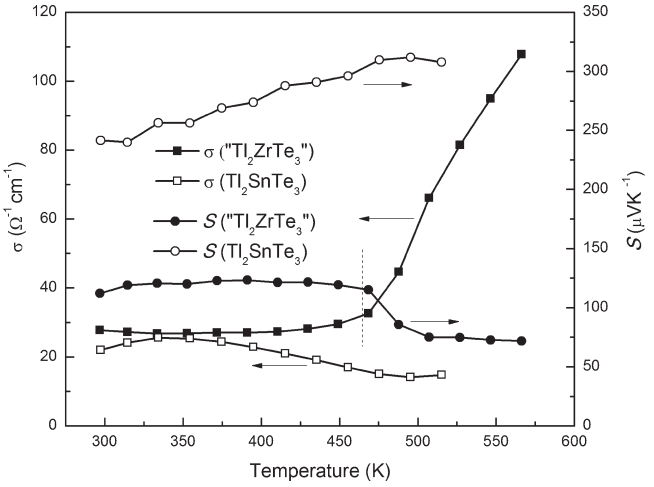

Figure 6. Temperature dependence of electrical conductivity and Seebeck coefficient of Tl_2ZrTe_3 and Tl_2SnTe_3. The dashed vertical line indicates the onset of the decomposition of Tl_2ZrTe_3.

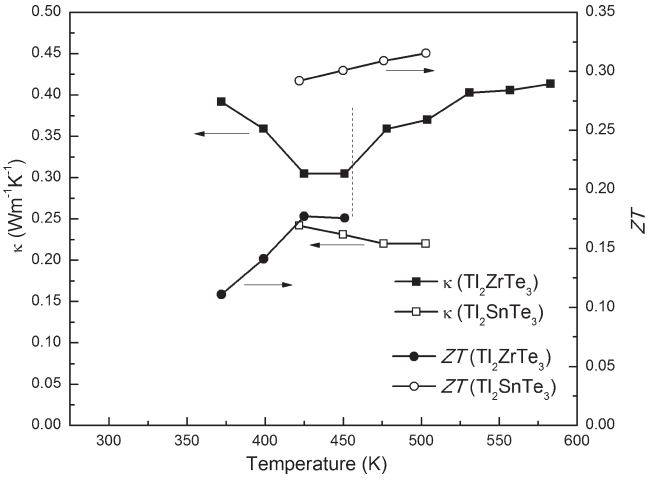

Figure 7. Temperature dependence of thermal conductivity and dimensionless figure of merit of Tl_2ZrTe_3 and Tl_2SnTe_3.

ribbons being separated by a layer of Tl atoms. Thus, the Tl atoms in Tl_2SnTe_3 have a higher coordination number than in Tl_2ZrTe_3, and the Sn atoms a smaller one, compared to Zr in Tl_2ZrTe_3.

Electronic Structure and Physical Properties. The densities of states (DOS) computed by the EHTB model exhibit an energy band gap (E_{gap}) of approximately 0.7 eV (Figure 4). In general, the EHTB estimated band gaps are overestimated, so that the experimental gap is likely smaller. The Tl 6s and Te 5p states contribute to the total DOS in the region below the Fermi level (E_F) with dominant Te contributions in the region between −16 eV and −13 eV, while the 4d states of Zr are dominant in the region above E_F, between −8.5 eV and −6.5 eV.

Tl_2SnTe_3 has a narrow indirect band gap of approximately 0.4 eV, as computed by the LMTO method (Figure 5), which typically underestimates the gap size. As in the case of Tl_2ZrTe_3, the upper region of the valence band is dominated by the Te 5p states. Noting that its unit cell contains 8 formula units, compared to 36 in case of Tl_2ZrTe_3, the peak above E_F is comparable to the one in the case of Tl_2ZrTe_3, when factoring in the smaller unit cell. On the other hand, the peak below E_F is larger per formula unit in the case of Tl_2SnTe_3, indicative of flatter bands and thus lower electrical conductivity and higher Seebeck coefficient.

The σ-T curve for Tl_2ZrTe_3 is basically temperature independent around 28 Ω^{-1} cm^{-1} until its decomposition temperature >450 K (vertical dashed line in Figure 6), where the steep increase is caused by the metallic character of the main product of the decomposition, Tl_5Te_3. Tl_2SnTe_3 also exhibits only minor changes with temperature, mostly a gentle decrease from 22 Ω^{-1} cm^{-1} to 15 Ω^{-1} cm^{-1} from room temperature to 515 K. The Seebeck coefficient (S) shows very little temperature dependence with values around +120 μV K^{-1} for the Zr compound until 450 K, and thereafter decreases because of the metallic character of then forming Tl_5Te_3. The corresponding room temperature values for Tl_4ZrTe_4 were +330 μV K^{-1} and 5.5 Ω^{-1} cm^{-1}. For Tl_2SnTe_3, S increases from +240 μV K^{-1} to +310 μV K^{-1} in the investigated temperature range.

The electrical conductivity (σ) of Tl_2SnTe_3 is slightly smaller than in case of Tl_2ZrTe_3 despite its higher relative density, which corresponds nicely to the different DOS, but could also be a consequence of a different charge carrier concentration. The nature of its σ-T and S-T curves is similar to the low temperature (below 300 K) thermoelectric properties of Tl_2SnTe_3 reported earlier, where comparable 300 K values of 171 μV K^{-1} and 14 Ω^{-1} cm^{-1} were observed on a sintered cold-pressed pellet.[13]

The power factor of Tl_2ZrTe_3 ($P.F. = S^2\sigma$) is almost independent of the temperature until its decomposition, ranging from 0.35 μW cm^{-1} K^{-2} to 0.41 μW cm^{-1} K^{-2}. For Tl_2SnTe_3, the power factor values continue to increase throughout the whole measured temperature range. The $P.F.$ values of these two materials, ranging from 0.2 μW cm^{-1} K^{-2} to <1.5 μW cm^{-1} K^{-2}, are small compared to advanced thermoelectrics, because of the rather low electrical conductivity. For example, $Fe_{0.05}Mo_3Sb_{5.4}Te_{1.6}$ attains 28 μW cm^{-1} K^{-2} at 950 K,[36] $Yb_{14}MnSb_{11}$ 6 μW cm^{-1} K^{-2} at 1200 K,[37] and Tl_9BiTe_6 10 μW cm^{-1} K^{-2} at 300 K.[6]

The total thermal conductivity (κ) of both compounds is shown in Figure 7. For Tl_2ZrTe_3, κ decreases from 0.39 W m^{-1} K^{-1} at 373 K to 0.30 W m^{-1} K^{-1} at 450 K, and for the Tl_2SnTe_3 sample, from 0.24 W m^{-1} K^{-1} at 420 K to 0.20 W m^{-1} K^{-1} at 500 K. The increase of the thermal conductivity of Tl_2ZrTe_3 above 450 K is a consequence of the beginning formation of metallic Tl_5Te_3 at the point. The values obtained are very low (in part caused by the porosity of 10% and 7%, respectively), advantageous for the thermoelectric energy conversion. This is somewhat typical for Tl tellurides, for example, Tl_9BiTe_6 with 0.4 W m^{-1} K^{-1} and Tl_4ZrTe_4 with 0.3 W m^{-1} K^{-1} at 300 K.

Finally, we have determined the thermoelectric efficiency of these materials in terms of their dimensionless figure of merit (ZT) from polynominal fits of the power factor and the thermal conductivity values (ignoring the data beyond the onset of the decomposition of Tl_2ZrTe_3). Tl_2ZrTe_3 has its maximum ZT value at 420 K with a value of 0.18. On the other hand, ZT increases with rising temperature for Tl_2SnTe_3, reaching a value of 0.31 at 500 K from 0.29 at 420 K (the highest and lowest temperature at which κ was determined). The maximum ZT value determined for Tl_2ZrTe_3 (0.18 at 420 K) is slightly larger than that for Tl_4ZrTe_4 (0.16 at 420 K).

■ CONCLUSIONS

We have synthesized and characterized the ternary compound Tl_2ZrTe_3. It possesses a large cubic unit cell with a = 19.118(1),

dx.doi.org/10.1021/cm200994t |Chem. Mater. 2011, 23, 3886–3891

space group $P2_13$, and $Z = 36$. The structure contains a 3D network of edge-sharing distorted [$ZrTe_6$] octahedra. The Tl atoms are also located in distorted octahedral coordination spheres of Te atoms. Interestingly, one of the Te sites is not in contact with any of the Zr atoms in the structure, but centers a [$TeTl_6$] octahedron. There are no significant Te−Te or Tl−Tl interactions, judged by the interatomic distances. Semiconducting compounds with such a huge unit cell, complex structure, and made of heavy elements usually have low thermal conductivity and are generally interesting from the viewpoint of thermoelectric properties. However, the fact that Tl_2ZrTe_3 decomposes around 450 K in an open system, even when protected by an inert gas atmosphere, inhibits the determination of its thermoelectric properties at higher temperatures.

We have studied the electronic structure of Tl_2ZrTe_3 via the EHTB calculation method. The electronic structure and the physical properties of Tl_2ZrTe_3 are compared with those of Tl_2SnTe_3. The latter has a calculated bad gap of 0.4 eV (LMTO method) and the former, 0.7 eV (EHTB method). Tl_2ZrTe_3 exhibits *p*-type semiconducting nature and shows a high Seebeck coefficient of around +120 $\mu V\ K^{-1}$ at 330 K. The dimensionless thermoelectric figure of merit, *ZT* of 0.18, was observed for Tl_2ZrTe_3 at 420 K. The temperature dependence of electrical conductivity and Seebeck coefficient of Tl_2SnTe_3 is more like that of a heavily doped semiconductor. The *ZT* values of Tl_2SnTe_3 are found to be higher at higher temperatures, reaching 0.31 at 500 K.

■ ASSOCIATED CONTENT

Supporting Information. One crystallographic information file (CIF) and one DSC plot. This material is available free of charge via the Internet at http://pubs.acs.org.

■ AUTHOR INFORMATION

Corresponding Author
*E-mail: kleinke@uwaterloo.ca.

■ ACKNOWLEDGMENT

Financial support from General Motors of Canada, the Ontario Centres of Excellence, and the Canada Research Chair program (CRC for H.K.) is appreciated. We gratefully acknowledge helpful discussions with Drs. J. R. Salvador, G. P. Meisner, and J. Yang from General Motors Research & Development Center, Warren, MI.

■ REFERENCES

(1) Snyder, G. J.; Toberer, E. S. *Nat. Mater.* **2008**, *7*, 105–114.
(2) Sootsman, J. R.; Chung, D. Y.; Kanatzidis, M. G. *Angew. Chem., Int. Ed.* **2009**, *48*, 8616–8639.
(3) Kleinke, H. *Chem. Mater.* **2010**, *22*, 604–611.
(4) Toberer, E. S.; May, A. F.; Snyder, G. J. *Chem. Mater.* **2010**, *22*, 624–634.
(5) Baxter, J.; Bian, Z. X.; Chen, G.; Danielson, D.; Dresselhaus, M. S.; Fedorov, A. G.; Fisher, T. S.; Jones, C. W.; Maginn, E.; Kortshagen, U.; Manthiram, A.; Nozik, A.; Rolison, D. R.; Sands, T.; Shi, L.; Sholl, D.; Wu, Y. Y. *Energy Environ. Sci.* **2009**, *2*, 559–588.
(6) Wölfing, B.; Kloc, C.; Teubner, J.; Bucher, E. *Phys. Rev. Lett.* **2001**, *86*, 4350–4353.
(7) Kurosaki, K.; Kosuga, A.; Yamanaka, S. *J. Alloys Compd.* **2003**, *351*, 14–17.
(8) Kurosaki, K.; Kosuga, A.; Yamanaka, S. *J. Alloys Compd.* **2003**, *351*, 279–282.
(9) Yamanaka, S.; Kosuga, A.; Kurosaki, K. *J. Alloys Compd.* **2003**, *352*, 275–278.
(10) Kurosaki, K.; Uneda, H.; Muta, H.; Yamanaka, S. *J. Alloys Compd.* **2004**, *376*, 43–48.
(11) Kosuga, A.; Kurosaki, K.; Muta, H.; Yamanaka, S. *J. Appl. Phys.* **2006**, *99*, 063705.
(12) Kosuga, A.; Kurosaki, K.; Muta, H.; Yamanaka, S. In *Materials and Technologies for Direct Thermal-to-Electric Energy Conversion*; Yang, J., Hogan, T. P., Funahashi, R., Nolas, G. S., Eds.; Materials Research Society: Warrendale, PA, 2006; Vol. 886, pp 343−347.
(13) Dichi, E.; Sghaier, M.; Kra, G. *J. Alloys Compd.* **2008**, *458*, 109–114.
(14) Bangarigadu-Sanasy, S.; Sankar, C. R.; Assoud, A.; Kleinke, H. *Dalton Trans.* **2011**, *40*, 862–867.
(15) Kuropatwa, B. A.; Assoud, A.; Kleinke, H. *J. Alloys Compd.* *509*, 6768−6772.
(16) Sankar, C. R.; Bangarigadu-Sanasy, S.; Assoud, A.; Kleinke, H. *J. Mater. Chem.* **2010**, *20*, 7485–7490.
(17) Sabov, M. Y.; Peresh, E. Y.; Barchii, I. E. *Ukr. Khim. Zh. (Russ. Ed.)* **1998**, *64*, 18–21.
(18) Agafonov, P. V.; Legendre, B.; Rodier, N.; Cense, J. M.; Dichi, E.; Kra, G. *Acta Crystallogr., Sect. C* **1991**, *47*, 1300–1301.
(19) Klepp, K. O.; Ecker, P. *J. Solid State Chem.* **1995**, *117*, 351–355.
(20) Klepp, K. O.; Kolb, A. *Z. Naturforsch. B* **1999**, *54*, 441–446.
(21) Keane, P. M.; Ibers, J. A. *J. Solid State Chem.* **1991**, *93*, 291–297.
(22) Mitchell, J. F.; Burdett, J. K.; Keane, P. M.; Ibers, J. A.; DeGroot, D. C.; Hogan, T. P.; Schindler, J. L.; Kannewurf, C. R. *J. Solid State Chem.* **1992**, *99*, 103–109.
(23) Mansuetto, M. F.; Keane, P. M.; Ibers, J. A. *J. Solid State Chem.* **1992**, *101*, 257–64.
(24) Klepp, K. O.; Gurtner, D. *J. Alloys Compd.* **1996**, *243*, 6–11.
(25) *APEX2*; Bruker AXS Inc.: Madison, WI, 2006.
(26) Spek, A. L. *J. Appl. Crystallogr.* **2003**, *36*, 7–13.
(27) Ren, J.; Liang, W.; Whangbo, M.-H. *CAESAR, Crystal and Electronic Structure Analyzer*; Prime-Color Software, Inc.: Raleigh, NC, 1998.
(28) Kang, D. B.; Jung, D.; Whangbo, M.-H. *Inorg. Chem.* **1990**, *29*, 257–259.
(29) Andersen, O. K. *Phys. Rev. B* **1975**, *12*, 3060–3083.
(30) Hedin, L.; Lundqvist, B. I. *J. Phys. C* **1971**, *4*, 2064–2083.
(31) Lambrecht, W. R. L.; Andersen, O. K. *Phys. Rev. B* **1986**, *34*, 2439–2449.
(32) Schewe, I.; Böttcher, P.; von Schnering, H. G. *Z. Kristallogr.* **1989**, *188*, 287–298.
(33) Assoud, A.; Soheilnia, N.; Kleinke, H. *J. Solid State Chem.* **2006**, *179*, 2707–2713.
(34) Assoud, A.; Soheilnia, N.; Kleinke, H. *Chem. Mater.* **2005**, *17*, 4509–4513.
(35) Zhang, X.; Schindler, J. L.; Hogan, T.; Albritton-Thomas, J.; Kannewurf, C. R.; Kanatzidis, M. G. *Angew. Chem., Int. Ed. Engl.* **1995**, *34*, 68–71.
(36) Xu, H.; Kleinke, K. M.; Holgate, T.; Rossouw, D.; Botton, G.; Tritt, T. M.; Kleinke, H. *J. Alloys Compd.* **2010**, *504*, 314–319.
(37) Brown, S. R.; Kauzlarich, S. M.; Gascoin, F.; Snyder, G. J. *Chem. Mater.* **2006**, *18*, 1873–1877.